Metamaterials and Antennas

Richard W. Ziolkowski

Contents

Introduction 288
Metamaterial-Based Antennas 290
Metamaterial-Inspired Antennas 293
  Electric NFRP, Electric Coupling 294
  Magnetic NFRP, Magnetic Coupling 297
  Magnetic NFRP, Electric Coupling 299
Multifunctional Electrically Small Antennas 301
  Multiband Antennas 301
  CP Antennas 305
  Multifunctional Designs 307
  Elemental Huygens Sources 308
Non-Foster Electrically Small Antennas 311
Summary 313
Cross-References 316
References 316

Abstract

A variety of antennas have been engineered with metamaterials and metamaterial-inspired constructs to improve their performance characteristics. Interesting examples include electrically small, near-field resonant parasitic (NFRP) antennas that require no matching network and have high radiation efficiencies. Experimental verification of their predicted behaviors has been obtained. This NFRP electrically small paradigm has led to a wide variety of multiband and multifunctional antenna systems. The introduction of active metamaterial constructs further augments the antenna designer's toolbox and leads to systems with many interesting and useful properties.

R.W. Ziolkowski (✉)
Department of Electrical and Computer Engineering, The University of Arizona, Tucson, AZ, USA
e-mail: ziolkowski@ece.arizona.edu

Z.N. Chen et al. (eds.), *Handbook of Antenna Technologies*,
DOI 10.1007/978-981-4560-44-3_14

Keywords
Artificial magnetic conductors • Bandwidth • Directivity • Electrically small antennas • Front-to-back ratio • Matching • Metamaterials • Non-Foster elements • Parasitics

Introduction

There has been a paradigm shift in recent years in the research on the physical properties of electromagnetic materials. This trend can be traced primarily to the development of metamaterials (MTMs) and their exotic physics properties and unusual engineering applications (Engheta and Ziolkowski 2006; Eleftheriades and Balmain 2005; Caloz and Itoh 2005). Metamaterials are artificial media whose basic unit cells are engineered in order that the overall composite possesses predesigned macroscopic physical properties which can be tailored for specific applications. By engineering the unit cell to a scale that is much smaller than the operating wavelength, the MTM exhibits homogenized material properties. MTMs are typically created by designing those inclusions to have resonant properties near a particular wavelength λ of interest, through either planar or volumetric loadings of space. They have provided extremely interesting flexibility in the engineering design processes for a variety of electromagnetic, acoustic, elastic, and thermal wave applications. Several electromagnetic prototypes have been developed for radiating and scattering applications operating from UHF to optical frequencies.

A generally accepted MTM classification scheme in terms of the effective permittivity and permeability of the MTM is shown in Fig. 1 (Engheta and Ziolkowski 2006). Materials normally occurring in nature are usually double positive (DPS). MTM interest in DPS characteristics is commonly connected with

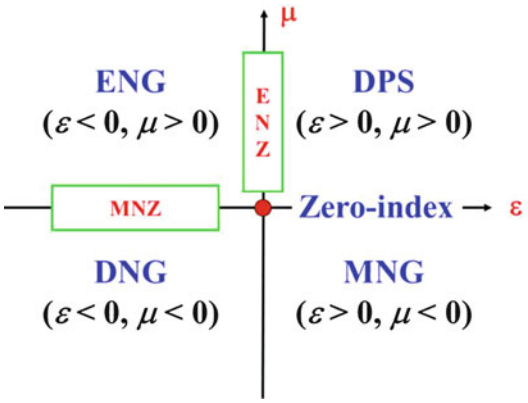

Fig. 1 Metamaterial classifications

desires to achieve permittivity or permeability values that are either large or less than one for either or both parameters. The double negative (DNG) metamaterials (MTMs), which are immediately associated with negative refraction effects, were proposed over 40 years ago (Veselago 1968). They were experimentally demonstrated at the turn of this century. Since then, a large variety of artificial material constructs have been designed, fabricated, and tested, confirming many of the exotic MTM properties (Smith et al. 2000; Ziolkowski 2003; Erentok and Ziolkowski 2007a; Engheta and Ziolkowski 2005).

The epsilon negative (ENG) and mu negative (MNG) MTMs are termed single negative (SNG), in direct contrast to the DNG cases. While the DPS and DNG MTMs allow propagating waves, all waves in SNG MTMs are evanescent. Extreme MTMs exhibit an extreme material or electromagnetic wave parameter. For instance, MTMs that have epsilon-near-zero (ENZ) or mu-near-zero (MNZ) characteristics also have a near-infinite or near-zero wave impedance. Zero-index MTMs have simultaneously zero permittivity and permeability and, thus, a zero index of refraction. Consequently, they exhibit spatially static (dynamic in time), infinite wavelength behaviors (Ziolkowski 2004).

The adaptation of a variety of epsilon-negative (ENG), mu-negative (MNG), and DNG metamaterials or simply metamaterial unit cells to achieve enhanced performance characteristics of antenna systems has since received considerable research attention. This includes studies, for instance, of small antennas (Ziolkowski and Kipple 2003, 2005; Qureshi et al. 2005; Stuart and Tran 2005, 2007; Stuart and Pidwerbetsky 2006; Ziolkowski and Erentok 2006, 2007; Erentok and Ziolkowski 2007a, b, c, 2008; Alici and Ozbay 2007; Arslanagić et al. 2007; Ziolkowski 2008a, b; Antoniades and Eleftheriades 2008; Lee et al. 2008; Greegor et al. 2009; Kim and Breinbjerg 2009; Ziolkowski et al. 2009a, b; Mumcu et al. 2009; Jin and Ziolkowski 2009, 2010a; Lin et al. 2010); multi-functional antennas (Sáenz et al. 2008; Herraiz-Martnez et al. 2009; Antoniades and Eleftheriades 2009; Jin and Ziolkowski 2010b, c, 2011; Lin et al. 2011; Zhu et al. 2010); infinite-wavelength antennas (Sanada et al. 2004; Lai et al. 2007; Park et al. 2007); patch antennas (Buell et al. 2006; Ikonen et al. 2007; Alú et al. 2007; Bilotti et al. 2008); leaky-wave antenna arrays (Eleftheriades and Balmain 2005; Caloz and Itoh 2005; Eleftheriades et al. 2007; Caloz et al. 2008); higher-directivity antennas (Enoch et al. 2002; Wu et al. 2005; Martinez et al. 2006; Franson and Ziolkowski 2009); low-profile antennas achieved with a variety of modified ground planes (Erentok et al. 2005; Erentok et al. 2007d; Yang and Rahmat-Samii 2009), e.g., artificial magnetic conductors (AMCs); and dispersion engineering of time-domain antennas (Caloz et al. 2008; Ziolkowski and Jin 2008). The proliferation of wireless devices for communication and sensor applications has restimulated interest in many different types of antennas. The often conflicting requirements of, for instance, efficiency, bandwidth, directivity, weight, and cost have made the design tasks onerous for antenna engineers with traditional schemes. The metamaterial-inspired engineering of antennas and their performance characteristics has provided an alternative approach to addressing these pressing issues.

Metamaterial-Based Antennas

The idea of using a resonant metamaterial object in the near field of an electrically small radiator to significantly enhance its performance was introduced in (Ziolkowski and Kipple, 2003; Ziolkowski and Kipple 2005; Ziolkowski and Erentok 2006; Erentok and Ziolkowski 2008) and reviewed in (Ziolkowski et al. 2011). The theoretical models began with enclosing a radiating dipole with double negative or single negative spherical metamaterial shells. For instance, nearly complete matching to a 50Ω source was achieved for a coax-fed dipole (loop) antenna within an ENG (MNG) or DNG shell without any external matching circuit, and high radiation efficiencies were realized giving overall (realized) efficiencies near 100 %. One of the original designs is shown in Fig. 2.

The physical explanation for this configuration is illustrated in Fig. 3. When an electrically small DPS sphere is illuminated by an electromagnetic wave, it responds as an electrically small dipole radiator, which is known to be a highly capacitive element. An electrically small shell also responds in this manner. However, if it is filled with an ENG material, its permittivity is negative, and, hence, its capacitance is negative. This means the shell acts as an inductive element. The combination of the lossy capacitive and inductive elements, i.e., the juxtaposition of the positive and negative material regions, yields a lossy (RLC) resonator.

The driven element, the electrically small dipole antenna, has a large negative reactance, i.e., it too is a capacitive element. Because the lossy resonator is in the extreme near field of the driven element, the fields involved and the subsequent responses are large. It was found that the reactance of this near-field resonant parasitic (NFRP) element, the resonant core-shell structure, can be conjugate

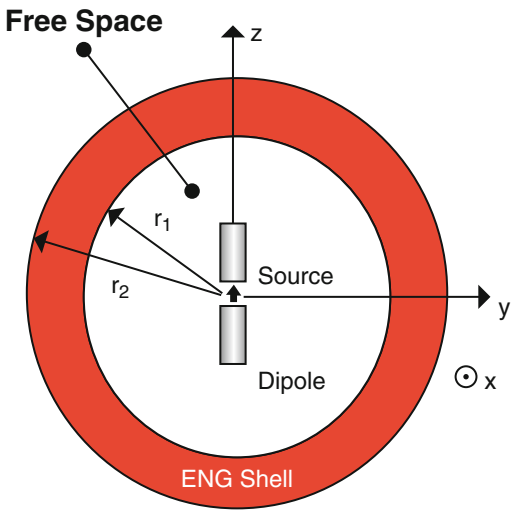

Fig. 2 Original metamaterial-based, efficient electrically small antenna consisting of a center-fed dipole antenna surrounded by an ENG shell

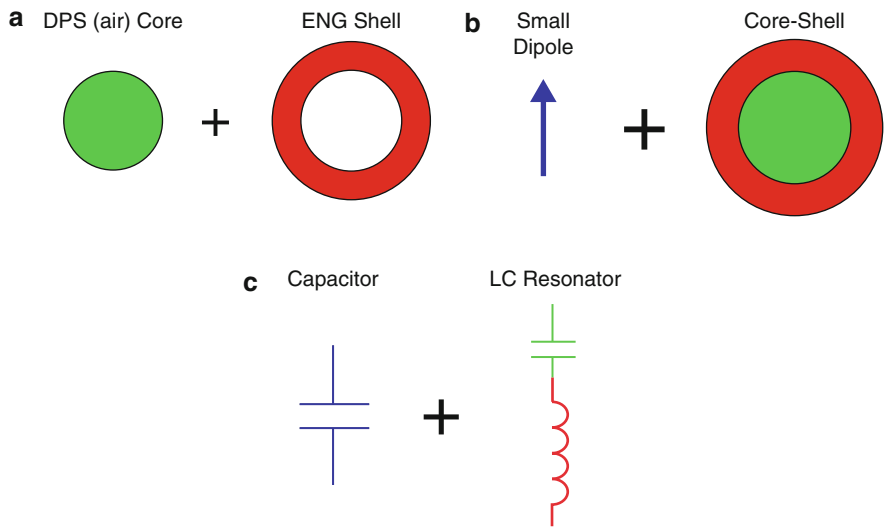

Fig. 3 The physics underlying the electrically small core shell configuration. (**a**) When excited, the DPS core acts as a small dipole element and, hence, is a capacitive element. The ENG shell responds as an electrically small dipole. However, because $\varepsilon < 0$ in the shell, it acts as an inductive element (**b**) Combining the core and shell, he resulting core-shell element acts like an LC resonator that can be matched to a driven electrically small dipole antenna, and (**c**) the circuit elements equivalent to the radiators in (**b**)

matched to the dipole reactance by adjusting their sizes and material properties to achieve an antenna resonance at

$$f_{res} = \frac{1}{2\pi} \frac{1}{\sqrt{L_{eff} C_{eff}}} \tag{1}$$

where L_{eff} and C_{eff} are, respectively, the effective inductance and capacitance of the system, in order to have the total reactance equal to zero (It is noted that in the dual case, a loop antenna and an MNG shell, the first antenna resonance is generally an antiresonance). Moreover, by tuning the effective capacitances and inductances of both the driven and parasitic elements, the entire antenna can be nearly completely matched to the source. Consequently, it can be said that the NFRP element acts as an impedance transformer.

Furthermore, by arranging the NFRP element so that the currents on it dominate the radiation process, high radiation efficiency and, consequently, very high overall efficiency, i.e., the ratio of the total radiated power to the total input power, can be realized. This basic physics of a NFRP element-based electrically small antenna is depicted in Fig. 4. On the other hand, the bandwidth remains commensurate with the electrical size of the antenna. It was demonstrated (Ziolkowski and Erentok 2007) that with an active ENG shell, the bandwidth could be increased considerably beyond the well-known Chu (1948) and Thal (2006) limits. The introduction of

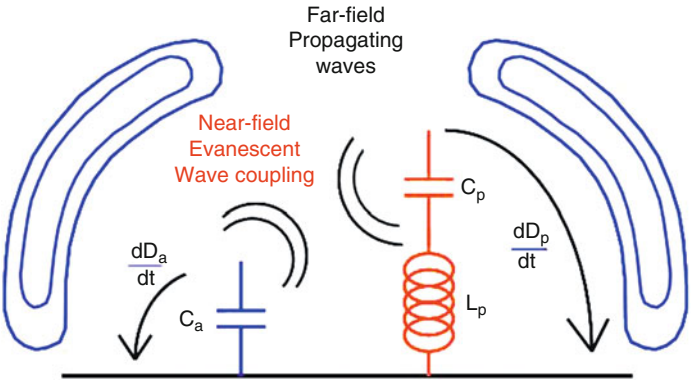

Fig. 4 The basic physics governing the behavior of an electrically small, near-field resonant (NFRP) antenna

non-Foster elements, which will be discussed later in this chapter, achieves this theoretical construct.

For example, the 300 MHz version of the dipole-ENG shell antenna shown in Fig. 2 was predicted to have an overall efficiency greater than 97 % when $ka = 0.12$ (Ziolkowski and Erentok 2006). It is noted, however, that because the antenna is electrically small, one would expect its directivity to be near that of a small dipole element, i.e., 1.76 dB. Furthermore, the bandwidth will be small. In particular, if a is the radius of the smallest sphere enclosing the entire antenna, $k = 2\pi/\lambda_{res} = 2\pi f_{res}/c$ is the free-space wavenumber at the resonance frequency, and RE is the radiation efficiency of the antenna, then the antenna is electrically small if $ka \leq 0.5$ (1.0) if a (no) ground plane is involved. The Chu lower bound on the quality factor of an electrically small antenna is (Best 2005)

$$Q_{lb} = RE \times \left[\frac{1}{(ka)^3} + \frac{1}{ka}\right] \tag{2}$$

giving $FBW_{ub} \approx 2/Q_{lb}$ as the upper bound of the half-power VSWR fractional bandwidth.

An important practical difficulty with the metamaterial-shell concept is the need to have extremely small unit cell sizes. For instance, if a $ka = 0.10$ antenna is desired, the thickness of the unit cell would be on the order of $\lambda_{res}/100$, thus requiring unit cells at least $\lambda_{res}/300$ in size to have three unit cells across the shell thickness and, consequently, something like a bulk metamaterial. Some of the smallest unit cells fabricated to date are $\lambda/75$ at 400 MHz (Erentok et al. 2007b). Furthermore, when there are losses associated with each unit cell, having many of them can lead to a large cumulative loss value. This behavior has been verified (Greegor et al. 2009) with a dual version of the system shown in Fig. 1. An antenna consisting of an electrically small driven magnetic loop and a mu-negative sphere was designed and fabricated. The measured results demonstrated that the MNG sphere did provide

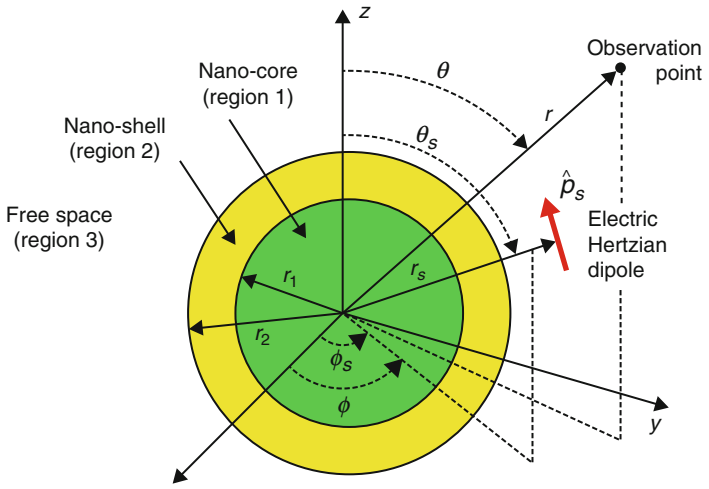

Fig. 5 Nano-antenna based on the NFRP paradigm

matching of the antenna to the source. However, because of the losses associated with each unit cell and because there were many cells involved in the overall design, it also did not achieve the expected high radiation efficiency.

There have been numerous other metamaterial-based antenna designs considered at RF frequencies. Electrically small antenna designs have been realized with small sets of unit cells and have been shown to have many potential applications (Dong and Itoh 2012). Moreover, the MTM-based NFRP paradigm has been extended to visible wavelengths, leading to active ENZ optical metamaterials (Gordon and Ziolkowski 2008), as well as passive and active nanoantenna (Arslanagić et al. 2007; Geng et al. 2011, 2012, 2013), nanolaser (Gordon and Ziolkowski 2007; Liberal et al. 2014), highly directive nanoantenna (Liberal et al. 2014; Arslanagić and Ziolkowski 2012), nanoamplifier (Arslanagić and Ziolkowski 2010; Arslanagić and Ziolkowski 2014), and quantum jammer (Arslanagić and Ziolkowski 2010, 2013, 2014) designs. The basic configuration is shown in Fig. 5. It results from the fact (Arslanagić et al. 2007) that the driven dipole antenna does not have to be internal to the resonant core-shell element to produce the enhanced total radiated power. As long as the dipole couples strongly with the resonator, the desired enhanced response occurs.

Metamaterial-Inspired Antennas

It was found (Erentok and Ziolkowski 2008) that a NFRP element constructed from a single MTM unit cell is sufficient to achieve the desired matching and high radiation efficiency properties. The resulting radiating systems were termed *metamaterial-inspired* antennas rather than metamaterial-based antennas because

only a single MTM unit cell was used and not a bulk medium. One does not need a large resonator around the entire radiating element but rather only a single unit cell – an electrically small resonator – in the near field of the driven radiator to achieve nearly complete matching to the source without any matching circuit and nearly 100 % overall efficiency. The initial designs made use of the analytical results that matched the type of driven element with the appropriate type of MTM. Both electric and magnetic coupling mechanisms between the driven and NFRP elements have since been explored. These metamaterial-inspired NFRP elements have led to a variety of interesting electrically small antenna systems. Several of these metamaterial-inspired NFRP designs have been fabricated and tested; the measured results are in good agreement with their simulated values.

Electric NFRP, Electric Coupling

The first NFRP antenna that was tested for its overall efficiency performance was the electric 2D EZ antenna shown in Fig. 6. The term *EZ* was chosen to reflect the fact that these original NFRP antennas were "easy" to design and fabricate. It was a Rogers Duroid^{TM} 5880 design. A monopole was printed on one side of the Duroid sheet and was coaxially fed through a copper ground plane. The NFRP element was a small meander line connected to the ground plane on the other side of the Duroid sheet. It has been demonstrated (Imhof et al. 2006; Imhof 2006) that this is a unit cell of an ENG MTM. It was demonstrated experimentally (Erentok and Ziolkowski 2008) that a 2D electric EZ antenna with $f_{res} = 1.37$ GHz and $ka \sim 0.49$ was nearly completely matched to the 50Ω source and had an overall efficiency ~94 %, with a

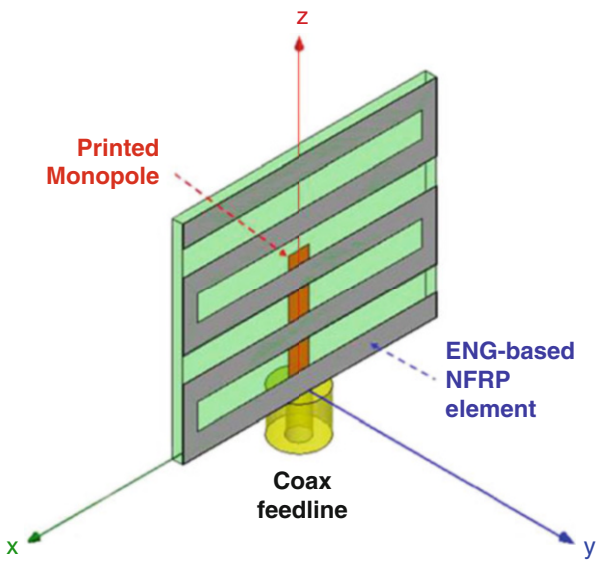

Fig. 6 ENG-based NFRP element, 2D electric EZ antenna

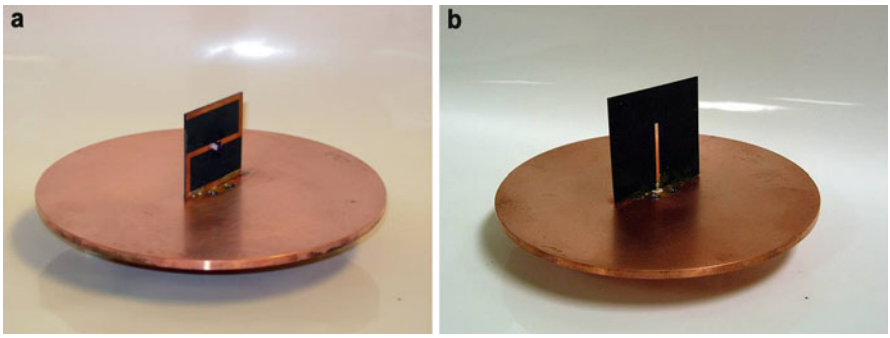

Fig. 7 Fabricated 570 MHz Z antenna on its small circular copper insert. (**a**) Z element side and (**b**) monopole element side

4.1 % fractional bandwidth. The NFRP element is electrically coupled to the driven monopole. The fields generated by the currents on the horizontal lines are nearly cancelled out by their images through the ground plane. The vertical elements radiate coherently and provide the high radiation efficiency.

With an interest to achieve an adjustable and potentially tunable version of this NFRP antenna, the Z antenna, whose 570 MHz, 31 mil, 2 oz Duroid 5880 realization is shown in Figs. 7a and b, was designed, fabricated by Boeing Research and Technology in Seattle, WA, and tested in the reverberation chambers at the National Institute of Science and Technology (NIST) in Boulder, CO (Ziolkowski et al. 2009b). The meander line was reduced to two simple J-elements connected with a lumped element inductor. The bottom J-element is connected to the ground plane. The monopole is coaxially fed through the ground plane. It was a 30 mm × 30 mm design incorporating a CoilCraft 47nH inductor. Measurements were taken with both the small ground plane version (120.6 mm diameter copper disk) shown in Fig. 7 and a larger ground plane version (the small ground plane version was inserted into an 18 in × 18 in = 457.2 mm × 457.2 mm copper ground plane). A physical comparison of the Z antenna and the reference ETS LINGREN 3106 double-ridged waveguide horn, which is about 94 % efficient in its 200 MHz-2GHz frequency band, is shown in Fig. 8. An overall efficiency equal to 80 % was measured at the resonance frequency $f_{res} = 566.2$ MHz ($ka = 0.398$) with a half-power fractional bandwidth $FBW = 3.0$ %, giving $Q = 4.03\ Q_{lb}$. There was little difference between the small ground plane and larger ground plane results. The predicted gain patterns in the small and large ground plane configurations are shown in Fig. 9, confirming that the Z antenna acts like a small vertical monopole with a finite ground plane. A second Z antenna, a 40 mm × 40 mm design incorporating a CoilCraft 169nH maxi inductor, had a 46 % measured overall efficiency at $f_{res} = 294.06$ MHz ($ka = 0.276$). Both sets of experimental results demonstrated, as predicted, the ability to obtain a lower resonance frequency with a simple redesign using a larger lumped element value. These experiments not only confirmed the predicted controllability of the

Fig. 8 Physical comparison of the 570 MHz small ground plane Z antenna and the dual-ridged reference horn in the NIST-Boulder reverberation chamber

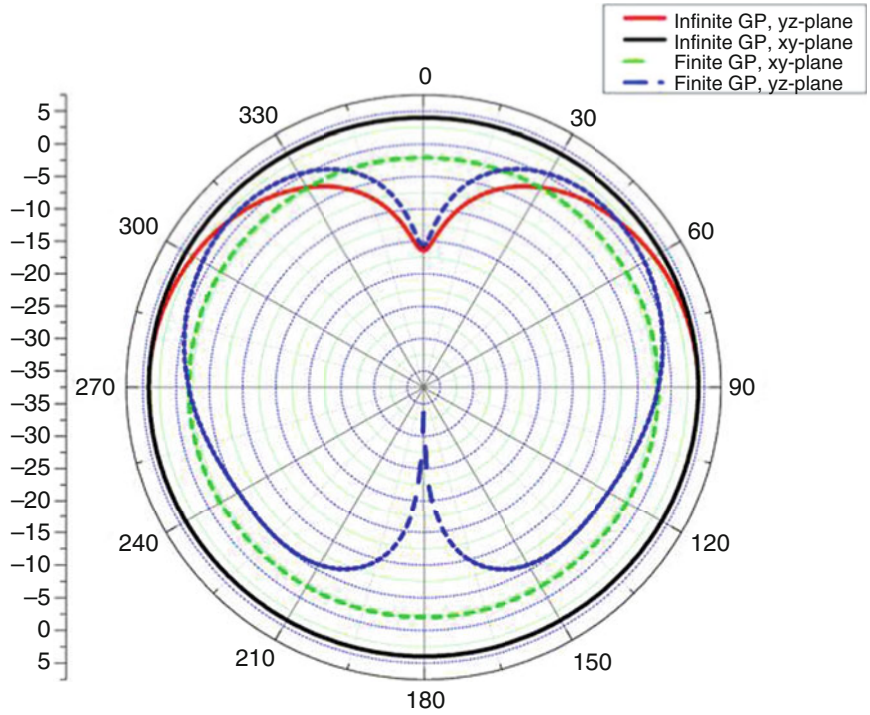

Fig. 9 HFSS-predicted patterns for the Z antenna at f_{res} have the expected electric monopole with a finite ground plane shapes

resonance frequency but also provided information on how to treat the lumped element inductor in the electromagnetic simulations. Based on these results, an updated Z antenna was designed with an overall efficiency of OE = 82.3 % ($|S_{11}|$ = −25.44 dB) at f_{res} = 285.6 MHz (ka = 0.428) (Ziolkowski et al. 2009b).

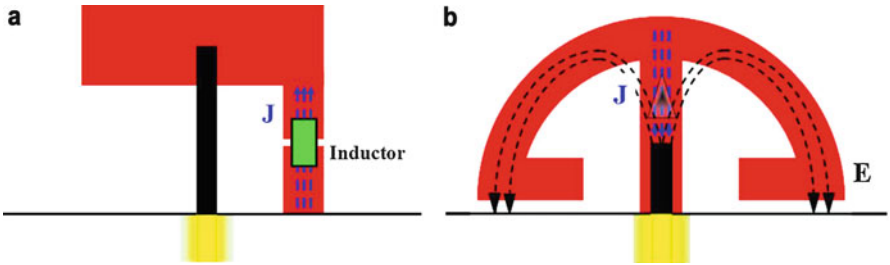

Fig. 10 Electrically small antenna designs incorporating generalized NFRP elements and coax-fed monopoles. (**a**) Rectangular NFRP with lumped element inductor, (**b**) Egyptian axe antenna with its distributed NFRP element. The current densities represent their basic behavior at the first resonance of the antenna

As it was recognized that the NFRP elements were the key to these electrically small designs, several variations have been designed to allow for other functionalities, which will be described below. For instance, the NFRP element associated with the Z antenna can be simplified considerably (Ziolkowski 2008a, b; Jin and Ziolkowski 2009; Jin and Ziolkowski 2011). The version shown in Fig. 10a consists of a split vertical segment connected by a lumped element inductor. The size of the upper horizontal metal rectangle is adjustable to tune the input reactance. HFSS simulations of the currents at the resonance frequency confirm that they are mainly on the vertical segments, which means this antenna radiates as a monopole over the ground plane and that the overall efficiency is above 90 % (Jin and Ziolkowski 2009). The second version in Fig. 10b utilizes a distributed NFRP element. The vertical strip couples directly to the driven monopole, the metal arc provides the inductance, and the horizontal strips provide additional capacitance. In resonance, HFSS simulations predict that the overall efficiency is above 90 % and confirm that the currents, as shown in Fig. 10b, are mainly on the vertical segment of the NFRP element, which again indicates why this antenna radiates as a monopole over the ground plane (Ziolkowski et al. 2011).

Magnetic NFRP, Magnetic Coupling

In a similar fashion, the NFRP element can be driven with the magnetic field of the driven element. In conjunction with the analytical solutions, a driven magnetic semiloop antenna coaxially fed through a finite ground plane was first considered. This led to the magnetic 2D and 3D EZ antennas (Erentok and Ziolkowski 2007a, b; Ziolkowski et al. 2009b; Lin et al. 2010). This feed-coupling scheme is graphically illustrated in Fig. 11, which illustrates a variation of the 2D magnetic EZ antenna. The parasitic element is a capacitively loaded loop (CLL), which was originally used successfully to achieve an artificial magnetic conductor metamaterial (without any ground plane) (Erentok et al. 2005). Both distributed and lumped element versions have been fabricated and tested successfully (Erentok and Ziolkowski 2008).

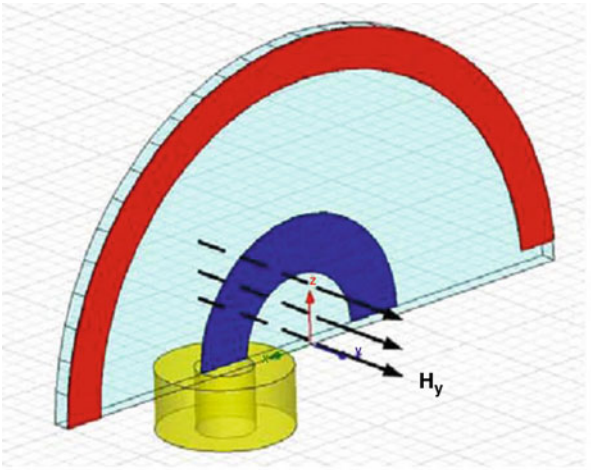

Fig. 11 The magnetic flux of the printed semi-loop antenna coaxially fed through a finite ground plane drives the CLL NFRP element in this variation of the 2D magnetic EZ antenna

The 3D magnetic EZ antenna is composed of an electrically small loop antenna that is coaxially fed through a finite ground plane and that is integrated with an extruded CLL element. This 3D CLL structure is designed to be the NFRP element. The measured results (Ziolkowski et al. 2009b) for the 3D magnetic EZ antenna demonstrated that for an electrical size, $ka \sim 0.43$, at 300.96 MHz, nearly complete matching to a 50 Ω source, and a high overall efficiency (>94 %) was achieved. These results and those in Erentok and Ziolkowski (2007b, c) established that the CLL-based elements can work in many frequency bands, e.g., from the ultrahigh-frequency (UHF) band to the X band. While negative permeability cannot be ascribed to either the 2D or 3D CLL elements themselves, a metamaterial constructed with them as its unit cell inclusion would exhibit MNG properties. Nonetheless, as with the electric source–electric coupling cases, it is the electrically small, magnetic-based NFRP CLL structure that provides the ability to match the electrically small loop antenna to the source. This can be visualized with the configuration dual to that shown in Fig. 4. The NFRP element again enhances the radiation process to achieve high radiation efficiencies. In particular, the CLL element can be engineered to control the strong magnetic flux generated by the small driven loop antenna and convert it into the appropriate currents flowing on the CLL element. Furthermore, this magnetic coupling process between the driven loop and the NFRP CLL element can be adjusted to tune the resonance of the entire antenna system according to Eq. 1 (Erentok and Ziolkowski 2008; Kim and Breinbjerg 2009). These metamaterial-engineered NFRP antennas again help overcome the loss issues associated with an actual metamaterial-based antenna design (Greegor et al. 2009). The wire versions of the CLL NFRP antennas have also been designed and show similar performance characteristics (Lin et al. 2011).

A similar low-profile (height ~ $\lambda_{res}/25$) 3D magnetic EZ antenna was designed for operation at 100 MHz. The fabricated antenna is shown in Fig. 12. The measured and simulated results were in very good agreement. This $ka = 0.46$ antenna was

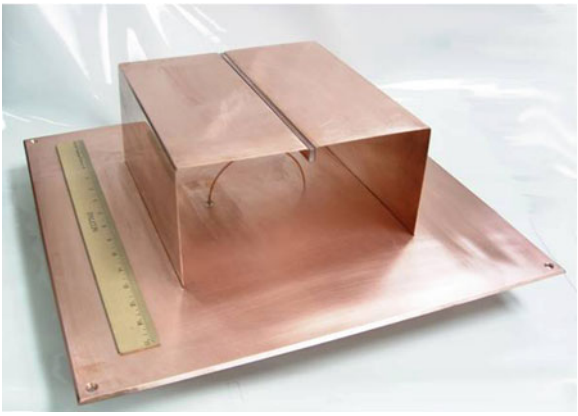

Fig. 12 The fabricated 100 MHz 3D magnetic EZ antenna in its small ground plane configuration

measured to have OE ~ 95 % and a half-power VSWR fractional bandwidth of 1.52 % ($Q = 11.06\ Q_{lb}$) at $f_{res} = 105.2$ MHz. This design utilized a quartz spacer ($\varepsilon_r = 3.78$) to help lower the resonance frequency and to provide mechanical stability during shipping and operation. Similar antennas have been designed for operation at 20 MHz using simply a $\varepsilon_r = 100$ spacer (Lin et al. 2010).

The corresponding HFSS-predicted gain patterns are shown in Fig. 13; the maximum gain value is 5.94 dB. Because the gain patterns are symmetric, it can be immediately inferred that the surface currents induced on the electrically small CLL element by the flux of the driven semiloop antenna are uniform and symmetric. This behavior is verified with the HFSS-predicted vector surface current distributions. This current distribution also demonstrates that this electrically small antenna system is radiating as a magnetic dipole over a finite ground plane (Lin et al. 2010).

Magnetic NFRP, Electric Coupling

Several important features distinguish the electric-based and the magnetic-based cases. The electric-based cases generally exhibit about half the Q values of the magnetic-based cases. Simply, the variation of the input impedance with frequency associated with a resonance is smaller than that associated with an antiresonance (Yaghjian and Best 2005). The electric-based cases radiate a vertical electric monopole type pattern; the magnetic-based cases radiate a horizontal magnetic dipole type pattern. The rate of decrease in the radiation efficiency as *ka* decreases is slower for the electric-based cases than for the magnetic-based ones. Because for many applications one would like broadside radiators and high radiation efficiencies for yet smaller *ka* values, antennas with a driven electric source have been investigated that are either magnetically or electrically coupled to a magnetic NFRP element. At first, because it deviated from the MTM-based analytical solution paradigm, this cross-design was not expected to yield a successful antenna. Fortunately it was, and it was found that it provides some interesting flexibilities for the multifunctional designs to be discussed below.

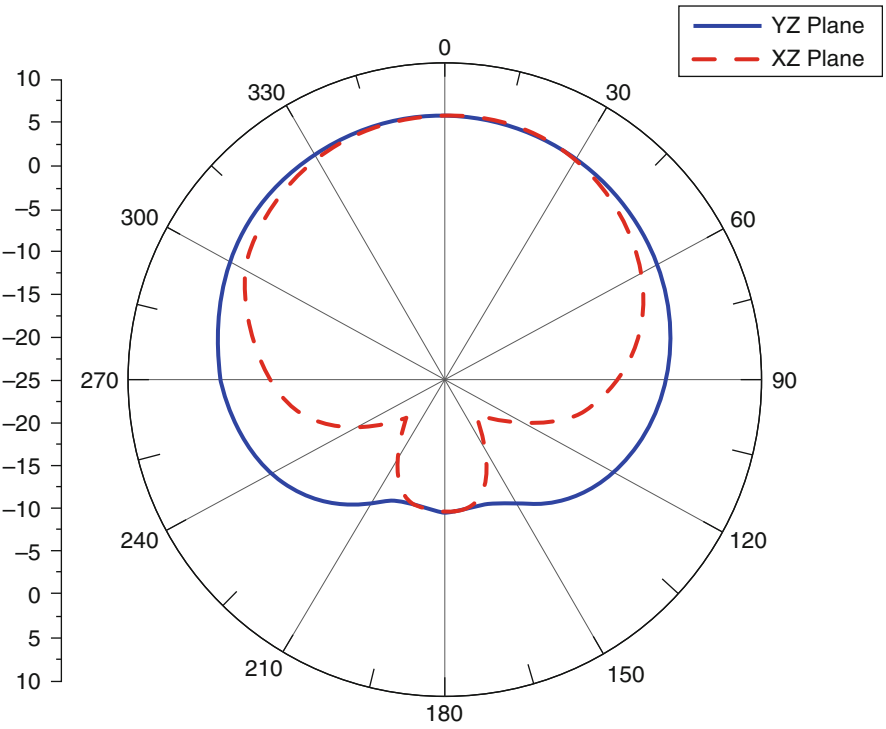

Fig. 13 E- and H-plane gain patterns for the 100 MHz 3D magnetic EZ antenna

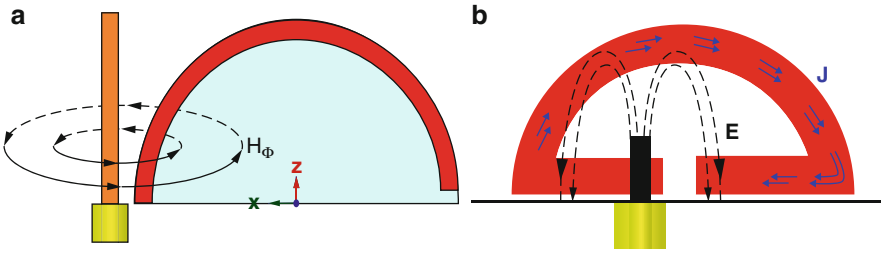

Fig. 14 Antenna composed of a driven electric source that is (**a**) magnetically coupled and (**b**) electrically coupled to a (magnetic) CLL-based NFRP element

The driven electric source, magnetically coupled design is illustrated in Fig. 14a. The magnetic field flux generated by the driven monopole is directly coupled to the CLL element. A realization of this design has been reported (Alici and Ozbay 2007). While it does produce a pattern with its maximum in the direction orthogonal to the plane, this magnetically coupled design is more sensitive and requires larger ka values to achieve nearly complete matching to the source than the corresponding electrically coupled design shown in Fig. 11b.

The protractor antenna (Jin and Ziolkowski 2011) illustrated in Fig. 14b has a thin gap between the horizontal legs of the CLL-based NFRP element and the ground plane. Because this NFRP element is in the extreme near field of the driven element, the electric fields across this gap are very large. Note that if the monopole were centered on the CLL element, the magnetic flux contributions would completely cancel because of symmetry; and the radiation process would be very weak from the electric field-generated currents along either side of the NFRP protractor element because a majority of them would be canceled by their images in the ground plane. However, by offsetting the monopole, the electric driven currents can form the desired loop mode around the CLL element. This loop mode radiates the desired magnetic dipole over a ground plane pattern. The coupling is strong, and consequently, the radiation efficiency can be large. Over 85 % overall efficiencies have been demonstrated for several protractor antennas (Jin and Ziolkowski 2010b; Jin and Ziolkowski 2011).

Multifunctional Electrically Small Antennas

Because of the known need for more functionality in a given antenna, the single antenna designs have been extended to multiantenna ones while trying to maintain the same footprint (overall size). By properly combining and phasing their effective electric and magnetic dipoles electrically small multiband, circular polarized (CP), elemental Huygens source and broader bandwidth antennas were obtained that are nearly completely matched to a 50Ω source and have high radiation efficiencies. These various designs are reviewed below.

Multiband Antennas

Several multiband antenna systems which consist of multiple NFRP elements in the very near field of the driven element, each being resonant at a specified, unique frequency, have been developed (Jin and Ziolkowski 2010c; Lin and Ziolkowski 2010). At each antenna resonance, only one or majorly one parasitic element efficiently radiates. It is worth pointing out that the directly driven monopole remains essentially nonradiating at all of the resonant frequencies. Impedance matching to the source at all multiband frequencies is achieved by adjusting the dimensions of each parasitic element and its distance from (and, hence, coupling to) the driven monopole. When there are multiple parasitic elements, the couplings among the parasitics also impact the radiation and matching processes. Efficient multiband operation results from properly understanding the effects of these multiple resonances and how to minimize their couplings. This NFRP approach is a distinct difference from the directly driven multiband dipole antennas proposed in Herraiz-Martnez et al. (2009) and related works that use parasitic split resonant rings to achieve the multiband capability. At each resonant frequency, the directly driven dipole plays a significant part in the radiation process, and the SRRs act as different

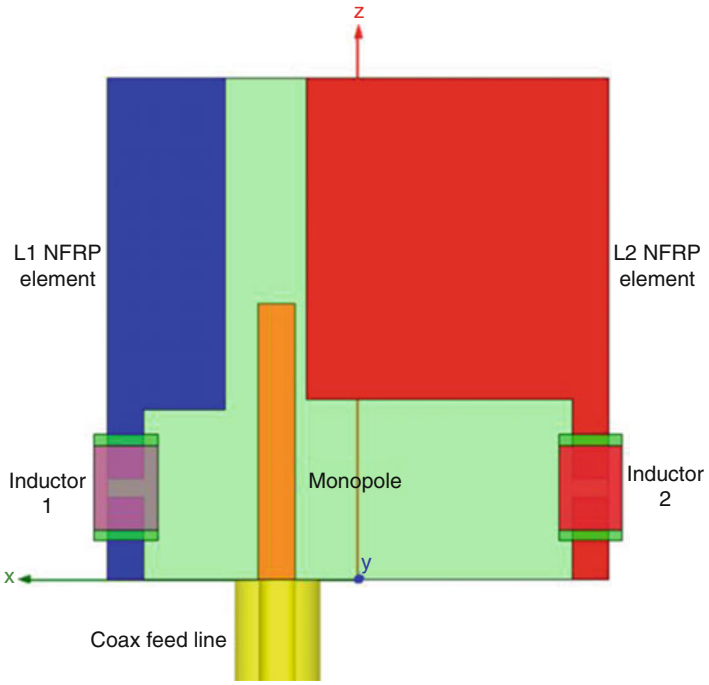

Fig. 15 Duroid 5880-based, single feed, dual-band NFRP antenna. This system has been designed, e.g., for the GPS L1 and L2 frequencies

loads at different resonant frequencies. Using the simplified NFRP element shown in Fig. 10a, the dual-band GPS L1 (1575.4 MHz) and L2 (1227.6 MHz) antenna shown in Fig. 15 was designed (Jin and Ziolkowski 2010c). In the same manner, a quad-band 430.0 MHz and GPS L1 (1575.42 MHz), L2 (1227.60 MHz), and L5 (1176.45 MHz) antenna was also designed (Jin and Ziolkowski 2010c).

The dual-band, asymmetric split EZ antenna system shown in Fig. 16 was designed to achieve a low-frequency dual-band system for low-earth-orbit satellite (LEOS) communications: 137.475 MHz uplink and 149.15 MHz downlink bands (Lin and Ziolkowski 2010). Note that these frequencies are separated by only 11 MHz. The radiation efficiencies for those resonant frequencies are 96.4 % and 71.5 %, respectively.

The reason why the higher resonant frequency has lower radiation efficiency is due to the currents being in opposition in these two CLL elements, i.e., they are out of phase. At the lower frequency, they are in phase. These EZ design results have provided us with the insight into the need for careful recognition of the relative current flows on the set of NFRP elements to achieve the highest possible radiation efficiencies. By controlling the relative phases of the currents, a related dual-band 429.8 MHz (SATCOM) and 1575.6 MHz (GPS L1) design, in which the two 3D CLL NFRP elements are nested and the semiloop antenna is diagonally oriented to

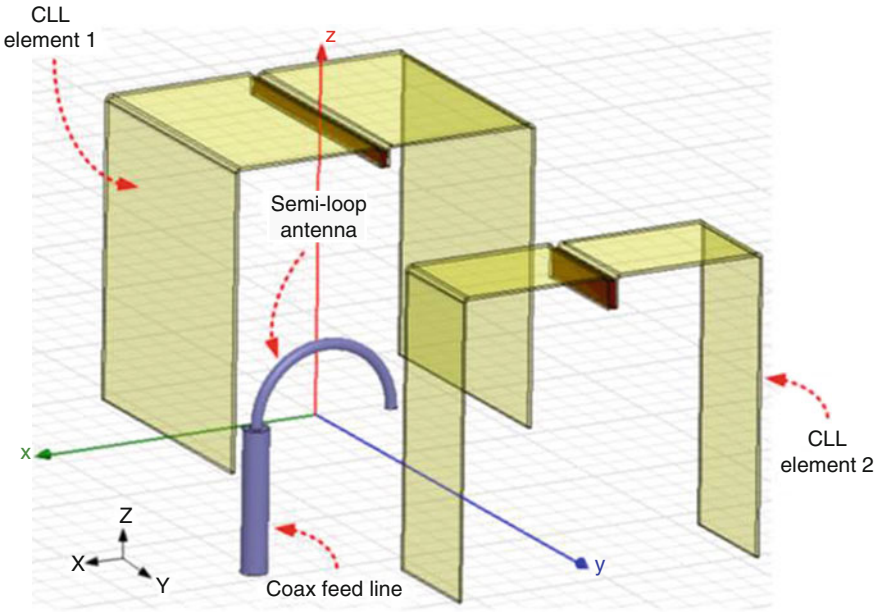

Fig. 16 A dual-band, asymmetric split, 3D magnetic EZ antenna for LEOS communications

excite each element, has radiation efficiencies of 83.8 % and 97.5 %, respectively (Lin and Ziolkowski 2010).

Another dual-band application is the desire to have both satellite positioning (GPS) and communications. Highly compact, multifunctional antennas that can communicate with satellites to accommodate both voice and data exchanges, while providing GPS functionality, are of great interest for portable communication device applications. For this reason, a dual-band GPS L1 (1575.42 MHz) and Global Star (GS, 1610–1621 MHz) electrically small, planar NFRP antenna shown in Fig. 17 was designed (Jin et al. 2012). This antenna has, by choice (Jin et al. 2012), a square footprint of 1.0×1.0 in^2. It was designed to be fabricated with the Rogers Duroid 4350 board material, which has a relative permittivity equal to 3.66, a loss tangent equal to 0.004, a 0.762-mm substrate thickness, and a 0.017-mm (0.5 oz) copper thickness.

To achieve the desired dual-band performance, two NFRP elements were incorporated with a single driven element. The two NFRP elements lie on one side of the Duroid sheet; the driven element, which is coaxially fed, lies on the other side. The NFRP elements are both top-loaded meander-line dipoles, which are rectangular variations of the circular Egyptian-axe dipole NFRP elements introduced in Jin and Ziolkowski (2010b). Both dipoles are the same except for the gaps between the capacitive loads, i.e., the capacitances formed by the gaps between the ends of the arrows. Because of the differences in the resulting capacitances, two independent resonant frequencies were obtained. However, to avoid any unnecessary structural

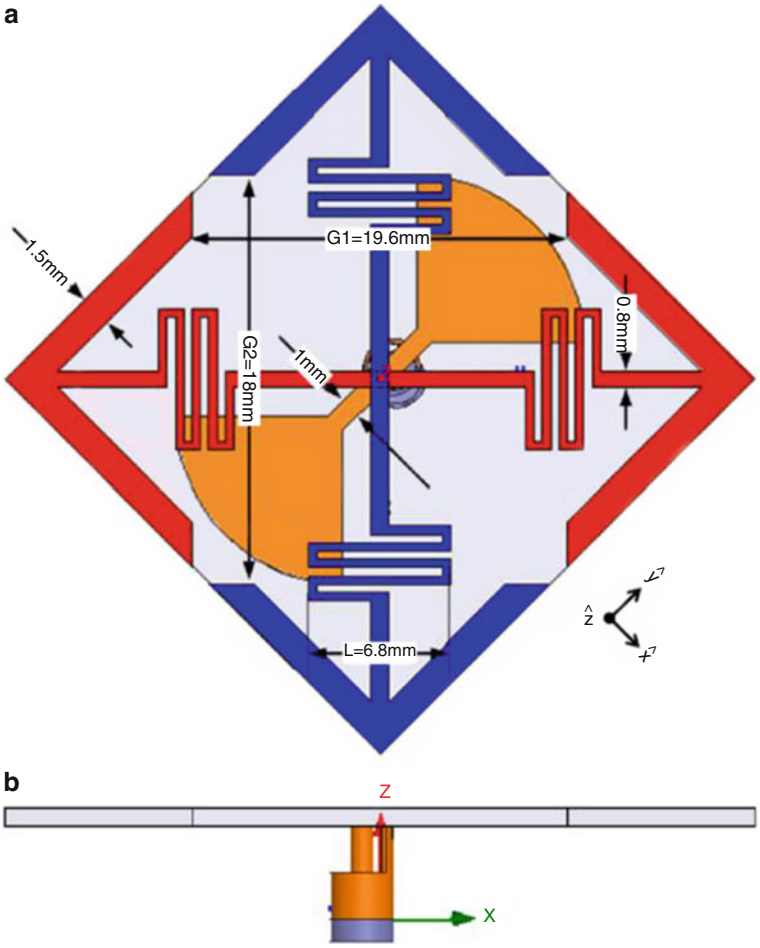

Fig. 17 Dual-band GPS L1/GS NFRP antenna with dimensions (in millimeters). (**a**) Top view. (**b**) Side view

overlaps and to keep the NFRP elements in a one-layer layout, the meander lines were introduced on their legs to increase the overall inductance while allowing a decrease in the requisite capacitances provided by their gaps and still maintaining the desired operating frequency. Furthermore, the NFRP elements are oriented orthogonal to each other. This necessitates the overlapping of these elements at the center of the square. It also required the introduction of the driven bowtie antenna (orange), which facilitates electric coupling to each NFRP element. Because the two dipoles are perpendicularly oriented, they operate essentially independently even though they are connected. The red (horizontal) dipole in Fig. 17a has a larger gap (G1) and is thus resonant at the GS band. The blue (vertical) dipole has a smaller gap (G2) and thus operates at the GPS L1 band.

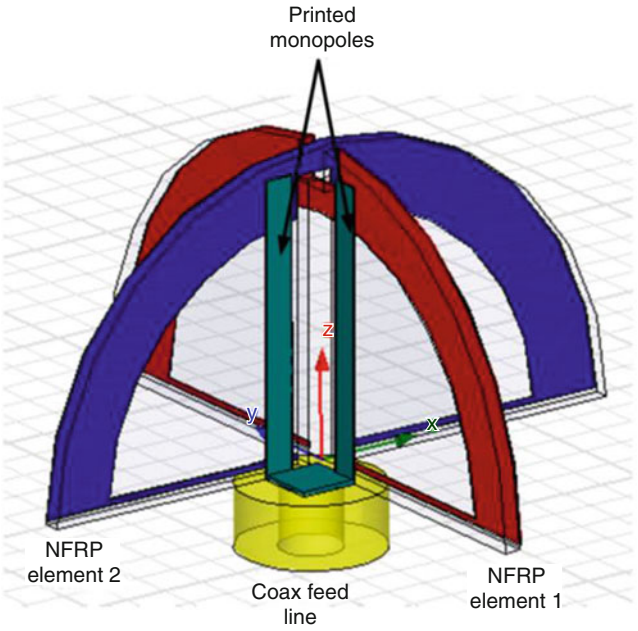

Fig. 18 CP protractor antenna. The CP behavior is achieved at a frequency between two closely spaced resonances through a 90° phase shift obtained between their input reactances

CP Antennas

Another functionality that has been added to the NFRP antenna paradigm is circular polarization (CP). In all of the cases noted above, the antennas are linearly polarized (LP). To achieve a CP system with a single feed in an electrically small package, one needs two orthogonal dipole radiators with an effective 90° phase shift between them. This behavior was realized with the protractor antenna system shown in Fig. 18. It is a GPS L1 CP design (Jin and Ziolkowski, 2011) with $a = 15$ mm; $f_{res} = 1575.4$ MHz giving $ka = 0.495$; a 89.2 % overall efficiency; a 29.3 MHz (−10 dB) bandwidth; a 7.2 MHz CP bandwidth; and an axial ratio equal to 0.26. Each protractor element produces a magnetic dipole parallel to the ground plane. One is tuned to be resonant below the desired operating frequency and thus creates an inductive reactance at it. The other is tuned to be resonant above the desired operating frequency and thus creates a capacitive reactance at it. Because these protractor NFRP elements are orthogonal to each other, their resonances can be tuned independently to generate the 90° phase shift between them necessary for the CP behavior.

Similarly, the planar (no ground plane) GPS L1 design shown in Fig. 19 was obtained (Jin and Ziolkowski 2010b). It has $ka = 0.539$ at 1575.4 MHz, an overall efficiency of 85 %, a 31.4 MHz (−10 dB) bandwidth, a 7.2 MHz CP bandwidth, and an axial ratio of 0.66. It makes use of the same phase shift paradigm but with two of

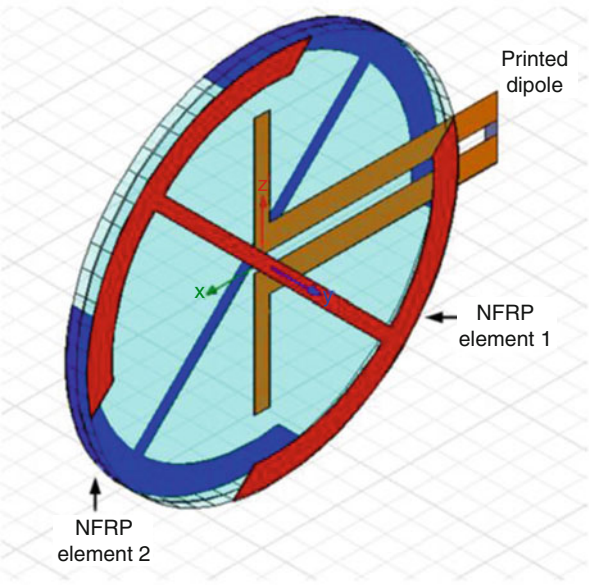

Fig. 19 A GPS L1 CP antenna consisting of two dipole NFRP elements and a driven printed dipole antenna. The CP behavior is achieved at a frequency between two closely spaced resonances through a 90° phase shift obtained between their input reactances. This Rogers Duroid™ 5880 design consists of three metal and two dielectric layers. The NFRP elements are on the outside faces of the dielectric layers; the printed dipole lies between those dielectric layers

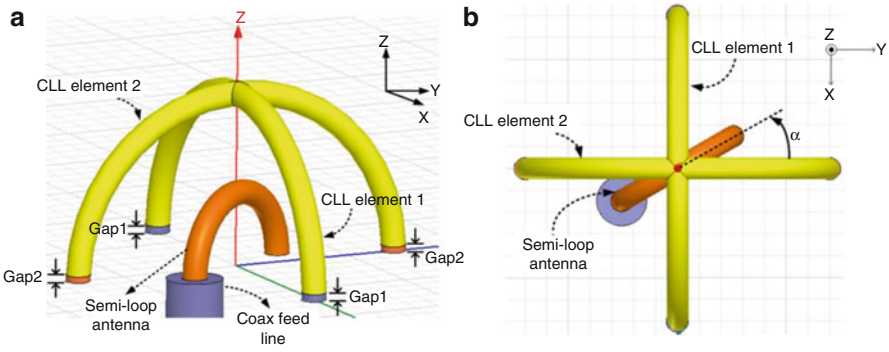

Fig. 20 Geometry of a GPS L1, CLL-based NFRP CP wire antenna whose coax-fed semi-loop is rotated α° with respect to the ZY-plane. The two CLL NFRP elements have two closely spaced resonances; the requisite 90° phase shift between their input reactances is obtained by tuning the angle α between the driven semi-loop antenna and the NFRP elements

the Egyptian axe NFRP elements shown in Fig. 14b and a driven printed dipole antenna. On the other hand, an electrically small wire, GPS L1 CP antenna, shown in Fig. 16, has been obtained (Lin et al. 2011) using two CLL-based wire NFRP elements driven by a coaxially fed semiloop antenna. It has $a = 15$ mm giving ka $= 0.495$ at $f_{res} = 1575.4$ MHz, a 96.9 % overall efficiency, a 30.7 MHz (-10 dB) bandwidth, a 7.9 MHz CP bandwidth, and an axial ratio of 0.6. The requisite phase shift is obtained by tuning the angle between the semiloop antenna and the NFRP elements (Fig. 20).

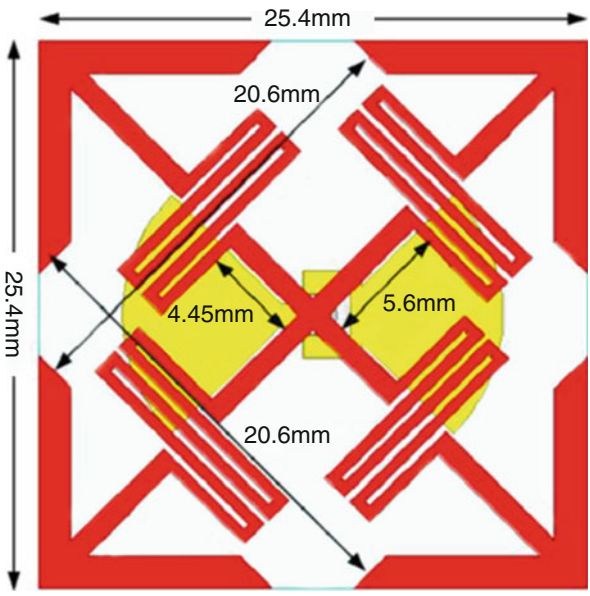

Fig. 21 Planar GPS L1 CP NFRP antenna

In the same manner, the GS/GPS antenna shown in Fig. 17 was modified to achieve the CP GPS-L1 version shown in Fig. 21, i.e., by simply tuning the resonances of each NFRP element to the requisite values. The axial ratio is minimum at 1.580 GHz with a value AR = 0.84. The overall efficiency at this frequency was 73.41 %. The corresponding peak directivity was (1.88 dB).

Multifunctional Designs

The multiband and CP aspects have been combined together (Jin and Ziolkowski 2011) into the dual-band GPS L1/L2 protractor antenna whose design is shown in Fig. 22a and whose fabricated prototype is shown in Fig. 22b. It was found possible to interleave two pairs of protractor NFRP elements with the appropriate phasing between the resonances to produce CP at both the GPS L1 and L2 frequencies with a single feed structure. As depicted in Fig. 22a, one can see in Fig. 22b the two pairs of protractor elements lying on two pieces of Rogers Duroid^{TM} 5880, which are oriented orthogonal to each other and to the finite copper ground plane. The initial experiments have demonstrated the basic operating principles, including the high overall efficiencies and the CP behavior (Jin and Ziolkowski 2011).

Planar multiband, CP GPS antennas have been obtained (Ta et al. 2012, 2013a, b, c) as variations of the designs shown in Figs. 17 and 21. The version shown in Fig. 23 covers the GPS L1–L5 bands. The primary radiating elements are two crossed printed dipoles, which incorporate a 90 phase delay line realized with a vacant-quarter printed ring to produce the CP radiation and broadband impedance matching. To achieve multiple resonances, each dipole arm is divided into four

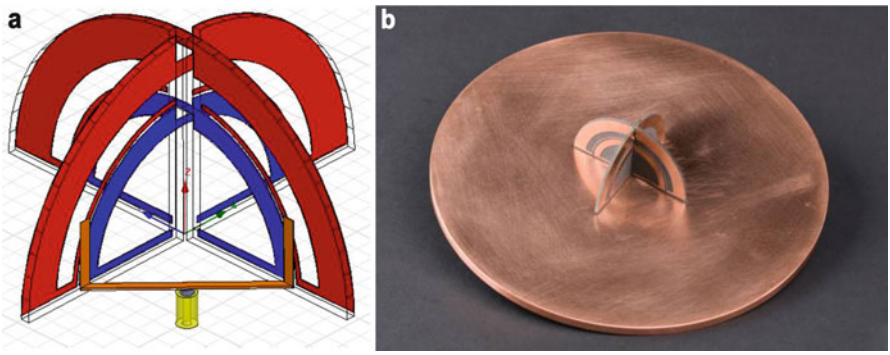

Fig. 22 Dual-band CP GPS L1/L2 NFRP antenna. (**a**) HFSS design (the L1 and L2 bands are associated, respectively, with the blue inside and red outside NFRP elements), (**b**) fabricated prototype

branches with different lengths, and a printed inductor with a barbed end is inserted in each branch to reduce the radiator size. An inverted, pyramidal, cavity-backed reflector is incorporated with the crossed dipoles to produce a unidirectional radiation pattern with a wide 3-dB axial ratio (AR) beamwidth and a high front-to-back ratio. This multiband CP antenna has broad impedance matching and 3-dB AR bandwidths covering the GPS L1–L5 bands.

Elemental Huygens Sources

Using the same NFRP element principles, an electrically small, elemental Huygens source can be obtained (Jin and Ziolkowski 2010b). It requires the combination of an electric and a magnetic dipole. A GPS L1 planar design that combines the Egyptian axe NFRP element for the electric dipole and two NFRP protractor elements to achieve a similar amplitude magnetic dipole is shown in Fig. 24a. It is a Rogers Duroid^{TM} 5880 design consisting of three metal and two dielectric layers. The NFRP elements lie on the outside faces of the dielectric layers; the driven printed dipole antenna lies between those dielectric layers. It has $ka = 0.46$ at $f_{res} = 1475$ MHz, a 85.9 % overall efficiency, and a 23.2 MHz (-10 dB) bandwidth. The HFSS-predicted 3D directivity pattern at this resonance frequency is shown in Fig. 18b. It has a maximum directivity of 4.5 dB and a 17.1 dB front-to-back ratio. The ideal maximum is 4.77 dB (i.e., a directivity of 3).

Using these concepts, a Huygens source nanoparticle laser has been designed (Liberal et al. 2014). The design is a three-layer, 120 nm outer-radius, nanoparticle consisting of a gain impregnated silicon core, a silver (ENG) shell surrounding it, and a gain impregnated silicon outer coating. At visible wavelengths, the high permittivity of silicon allows the appearance of a magnetic dipole mode in addition

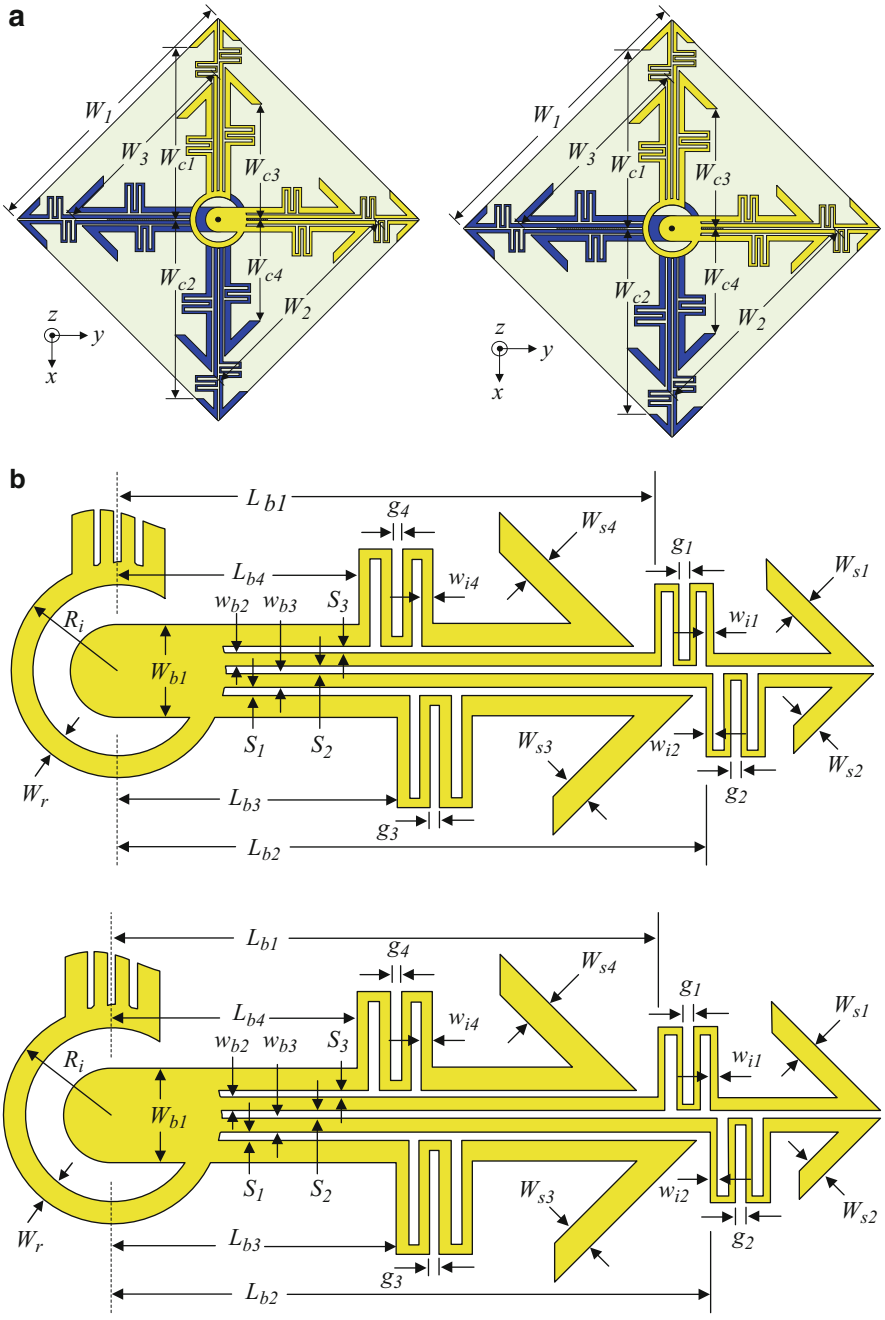

Fig. 23 (continued)

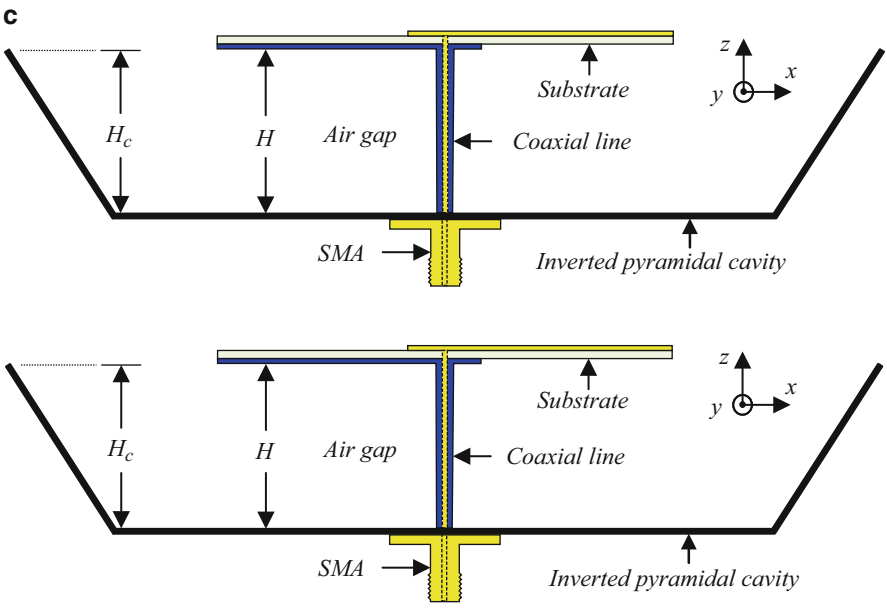

Fig. 23 Geometry of the multi-branch, asymmetrically barbed, crossed dipoles. (**a**) *Top view*; (**b**) vacant-quarter printed-ring and dipole arm; and (**c**) *side view*, including the cavity-backed reflector

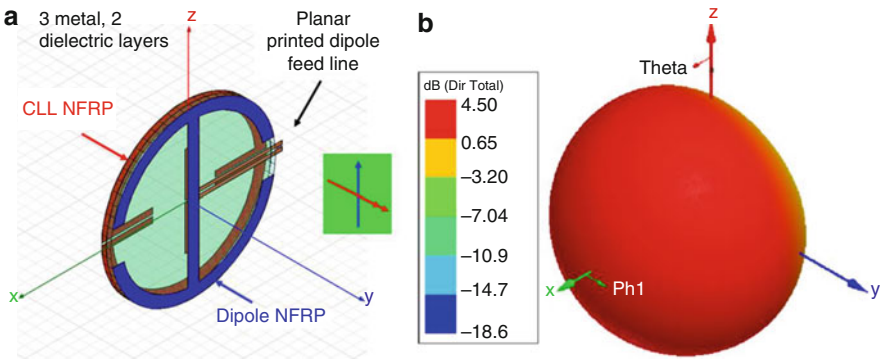

Fig. 24 An electrically small Huygens source that combines equal amplitude electric and magnetic dipoles and nearly achieves the maximum possible directivity. (**a**) HFSS design (the effective electric and magnetic dipoles are depicted in the insert), and (**b**) HFSS-predicted 3D directivity pattern

to the electric one. The former is associated with the outer shell; the latter with the core. By tuning the radius and gain constants, a proper balance of the electric and magnetic dipole modes is obtained. Lasing with a directivity of 3 in the forward scattering direction with respect to the exciting field occurs at 673.1 nm.

Non-Foster Electrically Small Antennas

As noted previously, there is an upper bound on the bandwidth of a passive electrically small antenna. As noted, recent efforts (Gustafsson et al. 2009; Yaghjian and Stewart 2010) have led to improved versions of the original Chu limit. Nevertheless, as Eq. 2 indicates, the fractional bandwidth basically decreases as $(ka)^3$ when ka becomes smaller. Moreover, it also indicates that one can obtain more bandwidth simply by reducing the radiation efficiency, i.e., by introducing more loss into the antenna. Another more complicated approach is to combine together multiple radiating elements with slightly different but overlapping resonance frequencies. It was found that some care must be exercised in this strategy. If the NFRP elements are too tightly coupled, the resonances tend to merge together and produce an even narrower bandwidth response. Moreover, it is usually difficult physically to squeeze several elements into an electrically small footprint. A variety of metamaterial-inspired electrically small antennas have been designed with Q factors that reach the fundamental bound (Best 2004, 2005, 2009; Kim et al. 2010; Kim 2010). Note, however, that even if an antenna reaches the upper bound, that bound is extremely small and the bandwidth cannot surpass it.

A method to overcome the passive bound is to introduce active elements into the antenna system. As shown in Fig. 25a, the standard approach (Aberle and Loepsinger-Romak 2007; Sussman-Fort and Rudish 2009) is to introduce an active matching circuit that produces the necessary resistance and reactance variations to maintain matching of the antenna to the source over a large bandwidth. Because of the sensitivity of active circuits, this becomes both a rather difficult design task and realization issue. In contrast, a metamaterial-inspired paradigm is to introduce the active element internally, integrating it with the NFRP element. This internal matching circuit approach, illustrated in Fig. 25b, has led to several successful designs (Jin and Ziolkowski 2010a; Zhu and Ziolkowski 2011, 2012a, b, 2013; White et al. 2012; Mirzaei and Eleftheriades 2013).

Consider the NFRP antenna shown in Fig. 26. This canopy antenna was designed (Jin and Ziolkowski 2010a) to approach the Chu-Thal limit. The legs of the canopy are lumped element inductors; the canopy is a copper spherical shell cap. With passive inductors, $ka = 0.047$ designs with $Q = 1.75\ Q_{Chu} = 1.17\ Q_{Thal}$ have been obtained with high overall efficiencies.

It was demonstrated further, as with the Z antennas, that the antenna resonances can be tuned over a frequency band with the same physical structure by varying only

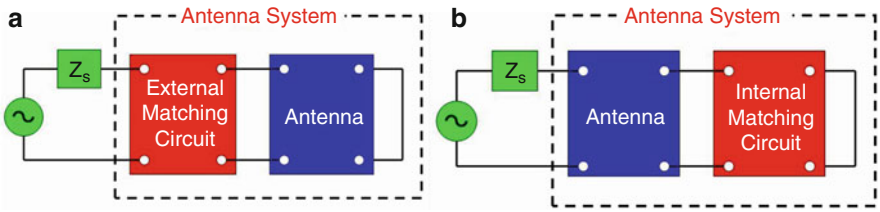

Fig. 25 Introducing active elements into an antenna system allows one to overcome the passive bounds on its bandwidth. (**a**) External active matching circuit, and (**b**) internal active matching element

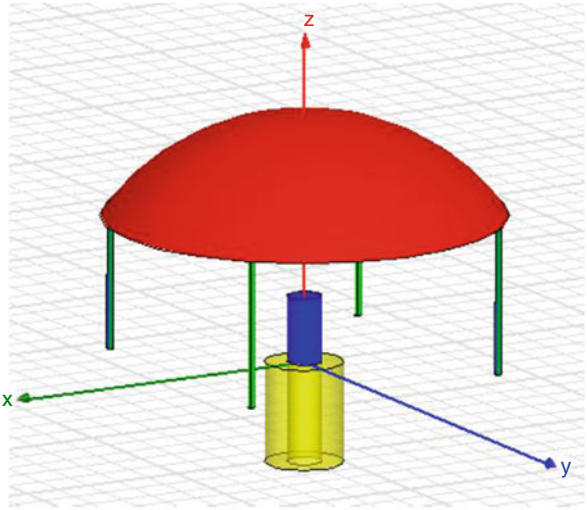

Fig. 26 Canopy antenna design. The NFRP element consists of four vertical legs (*green*), each being a lumped element inductor, and a copper spherical cap (*red*). The driven element is a monopole (*blue*) coaxially fed (*yellow*) through the ground (xy) plane. Efficient designs with $ka = 0.047$ at 300 MHz when the inductor is passive have bandwidths that approach the Chu-Thal limits and exhibit over 10 % bandwidth when an active inductor is used

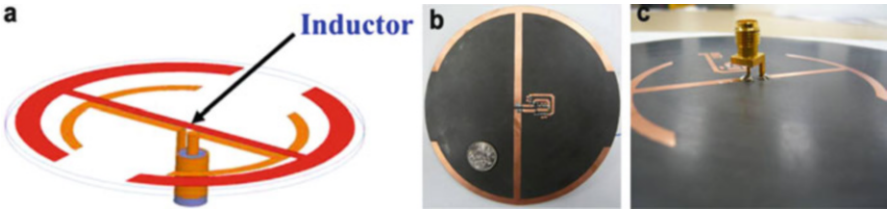

Fig. 27 Non-Foster-augmented Egyptian axe dipole (EAD) antenna to realize an efficient, electrically small antenna with large instantaneous impedance bandwidth. (**a**) Isometric view of the HFSS model, and (**b**) top and (**c**) bottom views of the fabricated and measured prototype

the value of the inductors. It was found that with this frequency-agile behavior, the inductor value decreases with an increasing resonance frequency, i.e., to achieve a larger instantaneous bandwidth, the inductor would have to be an active non-Foster element. Such an active inductor was designed with a Linvill-based negative impedance convertor (NIC) (Linvill 1953). HFSS simulations demonstrated a 10 % fractional bandwidth at 300 MHz was possible when $ka = 0.047$, nearly a thousandfold improvement over the passive design. This active design provides a different paradigm from the traditional non-Foster approaches. In principle, it requires only non-Foster reactive matching without any resistive matching. This simplifies the requirements on the active element considerably. This design is analogous to the original active analytical solution that produced a large fractional bandwidth for the idealized metamaterial-based, gain impregnated core-shell NFRP element, dipole-driven antenna system (Ziolkowski and Erentok 2007).

To test these non-Foster-augmented, metamaterial-inspired antenna concepts, the Egyptian axe dipole antenna shown in Fig. 27a was designed, fabricated, and

tested. A lumped element inductor, which is placed across the gap centered in the NFRP element, is treated as a tunable element. The $ka = 0.444$ EAD design for 300 MHz was obtained initially. Its frequency-agile behavior was then determined by varying the inductor value. The resulting non-Foster reactance was matched with a two-BJT Linvill NIC circuit. This circuit was then incorporated into the NFRP element as shown in Figs. 27b and c. The measured instantaneous impedance bandwidth was improved by a factor of 6.2 and was about a factor of 4 greater than the passive upper bound (Zhu and Ziolkowski 2012b, 2013). Similar performance improvements were obtained for a non-Foster-augmented protractor antenna (Zhu and Ziolkowski 2012a).

As with any active element, the stability of a non-Foster element is a significant practical issue. Component and fabrication tolerances can adversely affect the system enough that it will become unstable. It has been demonstrated that a key test of stability is to consider the time-domain response of the entire system – the non-Foster circuit and the antenna system augmented with it. Growth in time of any frequency component is an indicator of an instability. The stability of the NIC circuits and their integration with the EAD's radiating elements was confirmed in this manner before it was verified by experiment (Zhu and Ziolkowski 2013).

The internal non-Foster design paradigm has been extended to enhance not only the impedance bandwidth but also the directivity bandwidth (Tang et al. 2013). This was accomplished by introducing yet another NFRP element, augmenting it with a non-Foster element, and tuning it to act like an AMC surface. This approach also provided a solution to the holy grail of electrically small antennas: a design that exhibits simultaneously high efficiency, high directivity, impedance matching, and large front-to-back ratio (FTBR) over a broad instantaneous bandwidth. This antenna configuration is shown in Fig. 28 (Ziolkowski et al. 2013). The EAD antenna is augmented with an inductor-based NIC; it is integrated with a slot-modified parasitic disk that is augmented with a capacitor-based NIC.

The HFSS-simulated performance characteristics of this electrically small, $ka = 0.94$, system include a radiation efficiency > 81.63 %, directivity > 6.25 dB, FTBR > 26.71 dB over a 10.0 % fractional bandwidth. This yields a directivity-to-quality factor ratio which is greater than 10 times the fundamental upper bound: $(D/Q) > 10 \times (D/Q)_{\text{bare EAD}}$. These results are illustrated in Fig. 29. The directivity patterns in Fig. 29a have the characteristic cardioid pattern. This behavior persists over the bandwidth of the system. Consequently, it confirms that the parasitic disk acts as a broad-bandwidth AMC element. The other performance characteristics in Fig. 29b demonstrate a rather uniform behavior of the various performance characteristics over the entire bandwidth of the system.

Summary

As more has been learned about metamaterials and their electromagnetic properties, a variety of metamaterial-based and metamaterial-inspired antenna systems have been developed from RF to optical frequencies. Their metamaterial constructs have

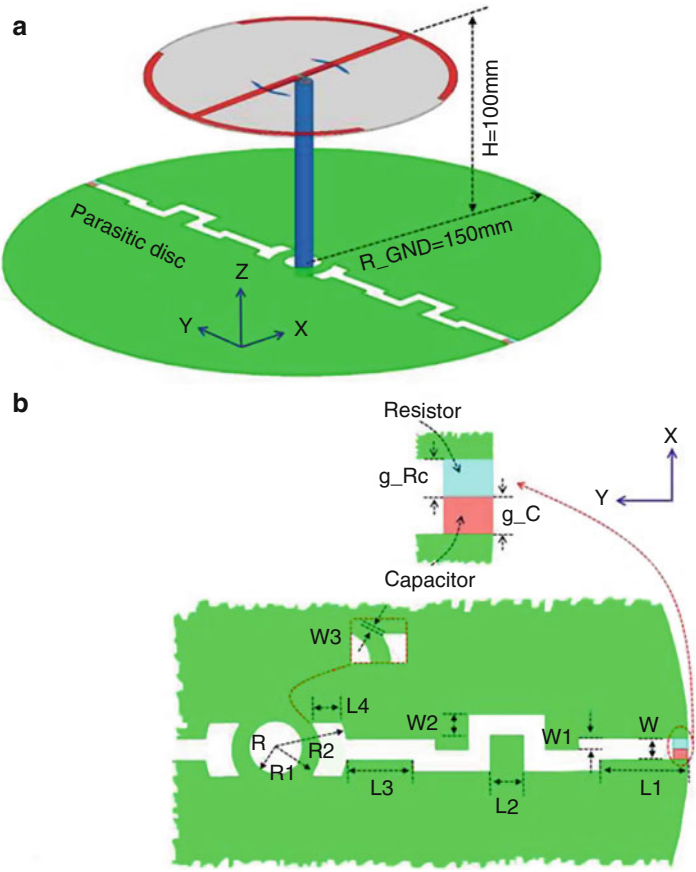

Fig. 28 EAD antenna integrated with a slot-modified, parasitic copper disk. (**a**) Isometric view, and (**b**) zoom-in view of one of the capacitor-augmented slot regions

led to enhanced performance characteristics. An electrically small antenna paradigm, the metamaterial-inspired near-field resonant parasitic (NFRP) antenna, is an example. It has provided realizations of a variety of interesting multifrequency, multifunctional designs whose input impedance can be nearly completely matched to the source and that exhibit high radiation efficiencies. The different coupling mechanisms between the driven and NFRP elements provide extra degrees of freedom to tailor the currents that produce the radiated fields. Both planar and volumetric loadings of space are possible with the NFRP elements, leading to more flexibility in antenna designs. The introduction of internal non-Foster elements provides a means to overcome the physical constraints associated with passive systems, e.g., a path to large instantaneous bandwidths. Moreover, the recognition that non-Foster-based elements can also be used to modify other antenna properties provides yet more design degrees of freedom. In particular, it allows one to design an

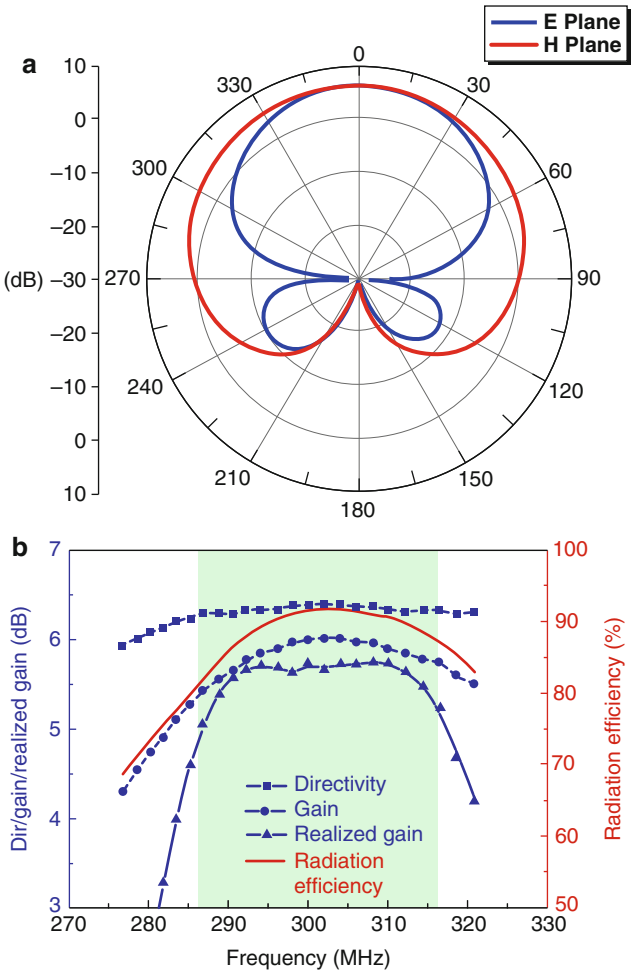

Fig. 29 Performance characteristics of the EAD antenna augmented with an inductive NIC and with a slot-modified, parasitic copper disk integrated with capacitive NICs. (**a**) E- and H-plane directivity patterns for the fully NIC-augmented EAD antenna at $f_{res} = 300$ MHz, and (**b**) simulated D, G, $G_{realized}$, and RE values versus the resonance frequency. The cyan shaded region represents, for easy reference, the instantaneous $BW_{10\ dB}$ region.

electrically small antenna with simultaneous high efficiency, high directivity, large front-to-back ratio, and nearly complete impedance matching over a large instantaneous bandwidth, i.e., active metamaterial constructs have provided the means to overcome the usually assumed performance characteristic trade-off approach to small antenna design.

At the heart of any wireless system is an antenna. Metamaterials, whether explicitly introduced into an antenna system as physical constructs or implicitly introduced using their often exotic properties to guide specifics of a design, have

provided exciting new opportunities to antenna engineers to meet the needs of a continually increasing demand for wireless products. Given slightly more than a decade of experience with the engineering applications of metamaterials, there is a great hope that they may be able to provide additional degrees of freedom for the design of many different forms of electromagnetic systems from DC to light.

Cross-References

► Physical Bounds of Antennas
► Theory of Transformation Optics in Antenna Design

References

Aberle JT, Loepsinger-Romak R (2007) Antenna with non-foster matching networks. Morgan & Claypool Publishers, San Rafael
Alici KB, Ozbay E (2007) Radiation properties of a split ring resonator and monopole composite. Phys Stat Sol (b) 244:1192–1196
Alú A, Bilotti F, Engheta N, Vegni L (2007) Subwavelength, compact, resonant patch antennas loaded with metamaterials. IEEE Trans Antennas Propag 55:13–25
Antoniades MA, Eleftheriades GV (2008) A folded-monopole model for electrically small NRI-TL metamaterial antennas. IEEE Ant Wireless Propag Lett 7:425–428
Antoniades MA, Eleftheriades GV (2009) A broadband dual-mode monopole antenna using NRI-TL metamaterial loading. IEEE Ant Wireless Propag Lett 8:258–261
Arslanagić S, Ziolkowski RW, Breinbjerg O (2007) Radiation properties of an electric Hertzian dipole located near-by concentric metamaterial spheres. Rad Sci 42:RS6S16
Arslanagić S, Ziolkowski RW (2010) Active coated nano-particle excited by an arbitrarily located electric Hertzian dipole – resonance and transparency effects. J Opt 12:024014
Arslanagić S, Ziolkowski RW (2012) Directive properties of active coated nano-particles. Advance Electromagn 1:57–64
Arslanagić S, Ziolkowski RW (2013) Jamming of quantum emitters by active coated nano-particles. IEEE J Sel Topics Quantum Electron 19:4800506
Arslanagić S, Ziolkowski RW (2014) Influence of active nano particle size and material composition on multiple quantum emitter enhancements: their enhancement and jamming effects. Prog Electromagn Res 149:85–99
Best SR (2004) The radiation properties of electrically small folded spherical helix antennas. IEEE Trans Antennas Propag 52:953–960
Best SR (2005) Low Q electrically small linear and elliptical polarized spherical dipole antennas. IEEE Trans Antennas Propag 53:1047–1053
Best SR (2009) A low Q electrically small magnetic (TE mode) dipole. IEEE Ant Wireless Propag Lett 8:572–575
Bilotti F, Alú A, Vegni L (2008) Design of miniaturized metamaterial patch antennas with μ-negative loading. IEEE Trans Antennas Propag 56:1640–1647
Buell K, Mosallaei H, Sarabandi K (2006) A substrate for small patch antennas providing tunable miniaturization factors. IEEE Trans Microw Theor Tech 54:135–146
Caloz C, Itoh T (2005) Electromagnetic metamaterials: transmission line theory and microwave applications. Wiley-IEEE, Hoboken
Caloz C, Itoh T, Rennings A (2008) CRLH traveling-wave and resonant metamaterial antennas. IEEE Ant Propag Mag 50:25–39
Chu LJ (1948) Physical limitations of omni-directional antennas. J Appl Phys 19:1163–1175

Dong Y, Itoh T (2012) Metamaterial-based antennas. Proc IEEE 100:2271–2285
Eleftheriades GV, Balmain KG (eds) (2005) Negative-refraction metamaterials fundamental principles and applications. Wiley-IEEE, Hoboken
Eleftheriades GV, Antoniades MA, Qureshi F (2007) Antenna applications of negative-refractive-index transmission-line structures. IET Microw Ant Propag 1:12–22
Engheta N, Ziolkowski RW (2005) A positive future for double negative metamaterials. IEEE Microwav Theor Tech 53:1535–1556
Engheta N, Ziolkowski RW (eds) (2006) Metamaterials: physics and engineering explorations. Wiley-IEEE Press, Hoboken, NJ
Enoch S, Tayeb G, Sabouroux Gúerin PN, Vincent P (2002) A metamaterial for directive emission. Phys Rev Lett 89:213902
Erentok A, Luljak PL, Ziolkowski RW (2005) Characterization of a volumetric metamaterial realization of an artificial magnetic conductor for antenna applications. IEEE Trans Ant Propag 53:160–172
Erentok A, Ziolkowski RW (2007a) A hybrid optimization method to analyze metamaterial-based electrically small antennas. IEEE Trans Ant Propag 55:731–741
Erentok A, Ziolkowski RW (2007b) An efficient metamaterial-inspired electrically-small antenna. Microw Opt Tech Lett 49:1287–1290
Erentok A, Ziolkowski RW (2007c) Two-dimensional efficient metamaterial-inspired electrically-small antenna. Microw Opt Tech Lett 49:1669–1673
Erentok A, Lee D, Ziolkowski RW (2007d) Numerical analysis of a printed dipole antenna integrated with a 3D AMC block. IEEE Ant Wireless Propag Lett 6:134–136
Erentok A, Ziolkowski RW, Nielsen JA, Greegor RB, Parazzoli CG, Tanielian MH, Cummer SA, Popa BI, Hand T, Vier DC, Schultz S (2007b) Low frequency lumped element-based negative index metamaterial. Appl Phys Lett 91:184104
Erentok A, Ziolkowski RW (2008) Metamaterial-inspired efficient electrically-small antennas. IEEE Trans Ant Propag 56:691–707
Franson SJ, Ziolkowski RW (2009) Confirmation of zero-N behavior in a high gain grid structure at millimeter-wave frequencies. IEEE Ant Wireless Propag Lett 8:387–390
Geng J, Ziolkowski RW, Jin R, Liang X (2011) Numerical study of active open cylindrical coated nano-particle antennas. IEEE Photon 3:1093–1110
Geng J, Ziolkowski RW, Jin R, Liang X (2012) Detailed performance characteristics of vertically polarized, cylindrical, active coated nano-particle antennas. Rad Sci 47, RS2013
Geng J, Jin R, Liang X, Ziolkowski RW (2013) Active cylindrical coated nano-particle antennas: polarization-dependent scattering properties. J Electromagnet Wave Appl (JEMWA). doi:10.1080/09205071.2013.809669
Gordon JA, Ziolkowski RW (2007) The design and simulated performance of a coated nano-particle laser. Opt Express 15:2622–2653
Gordon JA, Ziolkowski RW (2008) CNP optical metamaterials. Opt Express 16:6692–6716
Greegor RB, Parazzoli CG, Nielsen JA, Tanielian MH, Vier DC, Schultz S, Holloway CL, Ziolkowski RW (2009) Demonstration of impedance matching using a mu-negative (MNG) metamaterial. IEEE Ant Wireless Propag Lett 8:92–95
Gustafsson M, Sohl C, Kristensson G (2009) Illustrations of new physical bounds on linearly polarized antennas. IEEE Trans Antennas Propag 57:1319–1327
Herraiz-Martnez J, Garca-Muoz LE, Gonzlez-Ovejero D, Gonzlez-Posadas V, Segovia-Vargas D (2009) Dual-frequency printed dipole loaded with split ring resonators. IEEE Ant Wireless Propag Lett 8:137–140
Ikonen PMT, Alitalo P, Tretyakov SA (2007) On impedance bandwidth of resonant patch antennas implemented using structures with engineered dispersion. IEEE Ant Wireless Propag Lett 6:186–190
Imhof PD, Ziolkowski RW, Mosig JR (2006) Highly isotropic, low loss epsilon negative (ENG) unit cells at UHF frequencies. In: Proc European conference on antennas and propagation, EuCAP2006, European Space Agency, Noordwijk, The Netherlands, ESA SP-626, pp 552

Imhof PD (2006) Metamaterial-based epsilon negative (ENG) media: analysis and designs. Ecole Polytechnique Fédérale de Lausanne (EPFL) Master Thesis, Lausanne, Switzerland
Jin P, Ziolkowski RW (2009) Low Q, electrically small, efficient near field resonant parasitic antennas. IEEE Trans Ant Propag 57:2548–2563
Jin P, Ziolkowski RW (2010a) Broadband, efficient, electrically small metamaterial-inspired antennas facilitated by active near-field resonant parasitic elements. IEEE Trans Ant Propag 58:318–327
Jin P, Ziolkowski RW (2010b) Metamaterial-inspired, electrically small Huygens sources. IEEE Ant Wireless Propag Lett 9:501–505
Jin P, Ziolkowski RW (2010c) Multiband extensions of the electrically small metamaterial-engineered Z antenna. IET Microwav Ant Propag 4:1016–1025
Jin P, Ziolkowski RW (2011) Multi-frequency, linear and circular polarized, metamaterial-inspired near-field resonant parasitic antennas. IEEE Trans Ant Propag 59:1446–1459
Jin P, Lin CC, Ziolkowski RW (2012) Multifunctional, electrically small, conformal near-field resonant parasitic antennas. IEEE Ant Wireless Propag Lett 11:200–204
Kim OS, Breinbjerg O (2009) Miniaturized self-resonant split-ring resonator antenna. Electronics Lett 45:196–197
Kim OS, Breinbjerg O, Yaghjian AD (2010) Electrically small magnetic dipole antennas with quality factors approaching the Chu lower bound. IEEE Trans Ant Propag 58:1898–1906
Kim OS (2010) Low-Q electrically small spherical magnetic dipole antennas. IEEE Trans Ant Propag 58:2210–2217
Lai A, Leong MKH, Itoh T (2007) Infinite wavelength resonant antennas with monopolar radiation pattern based on periodic structures. IEEE Trans Ant Propag 55:868–876
Lee DH, Chauraya A, Vardaxoglou Y, Park WS (2008) A compact and low-profile tunable loop antenna integrated with inductors. IEEE Ant Wireless Propag Lett 7:621–624
Liberal I, Ederra I, Gonzalo R, Ziolkowski RW (2014) Induction theorem analysis of resonant nanoparticles: design of a Huygens source nanoparticle laser. Phys Rev Appl 1:044002
Lin CC, Ziolkowski RW, Nielsen JA, Tanielian MH, Holloway CL (2010) An efficient, low profile, electrically small, VHF 3D magnetic EZ antenna. Appl Phys Lett 96:104102
Lin CC, Ziolkowski RW (2010) Dual-band 3D magnetic EZ antenna. Microw Opt Tech Lett 52:971–975
Lin CC, Jin P, Ziolkowski RW (2011) Electrically small dual-band and circularly polarized magnetically-coupled near-field resonant parasitic wire antennas. IEEE Trans Ant Propag 59:714–724
Linvill JG (1953) Transistor negative-impedance converters. Proc IRE 41:725–729
Martinez A, Piqueras MA, Marti J (2006) Generation of highly directional beam by k-space filtering using a metamaterial flat slab with a small negative index of refraction. Appl Phys Lett 89:131111
Mirzaei H, Eleftheriades GV (2013) A resonant printed monopole antenna with an embedded non-Foster matching network. IEEE Trans Ant Propag 61:5363–5371
Mumcu G, Sertel K, Volakis JL (2009) Miniature antenna using printed coupled lines emulating degenerate band edge crystals. IEEE Trans Ant Propag 57:1618–1624
Park J-H, Ryu YH, Lee JG, Lee JH (2007) Epsilon negative zeroth-order resonator antenna. IEEE Trans Ant Propag 55:3710–3712
Qureshi F, Antoniades MA, Eleftheriades GV (2005) Compact and low-profile metamaterial ring antenna with vertical polarization. IEEE Ant Wireless Propag Lett 4:333–336
Sáenz E, Gonzalo R, Ederra I, Vardaxoglou JC, de Maagt P (2008) Resonant meta-surface superstrate for single and multifrequency dipole antenna arrays. IEEE Trans Ant Propag 56:951–960
Sanada A, Kimura M, Awai I, Caloz C, Itoh T (2004) A planar zeroth-order resonator antenna using a left-handed transmission line. In: Proc. 34th European Microwave Conference, Amsterdam, The Netherlands, pp 1341–1344

Smith DR, Padilla WJ, Vier DC, Nemat-Nasser SC, Schultz S (2000) Composite medium with simultaneously negative permeability and permittivity. Phys Rev Lett 84:4184–4187

Stuart HR, Tran C (2005) Subwavelength microwave resonators exhibiting strong coupling to radiation modes. Appl Phys Lett 87:151108

Stuart HR, Pidwerbetsky A (2006) Electrically small antenna elements using negative permittivity resonators. IEEE Trans Ant Propag 54:1664–1653

Stuart HR, Tran C (2007) Small spherical antennas using arrays of electromagnetically coupled planar elements. IEEE Ant Wireless Propag Lett 6:7–10

Sussman-Fort SE, Rudish RM (2009) Non-Foster impedance matching of electrically-small antennas. IEEE Trans Ant Propag 57:2230–2241

Ta SX, Park I, Ziolkowski RW (2012) Dual-band wide-beam crossed asymmetric dipole antenna for GPS applications. Electronic Lett 48:1580–1581

Ta SX, Park I, Ziolkowski RW (2013a) Circularly polarized crossed dipole on an HIS for 2.4/5.2/5.8-GHz WLAN applications. IEEE Ant Wireless Propag Lett 12:1464–1467

Ta SX, Park I, Ziolkowski RW (2013b) Multi-band, wide-beam, circularly polarized, crossed asymmetrically barbed arrowhead dipole antenna for GPS applications. IEEE Trans Ant Propag 61:5771–5775

Ta SX, Han JJ, Park I, Ziolkowski RW (2013c) Wide-beam circularly polarized crossed scythe-shaped dipoles for global navigation satellite systems. J Electromagn Eng Sci 13:224–232

Tang MC, Zhu N, Ziolkowski RW (2013) Augmenting a modified Egyptian axe dipole antenna with non-Foster elements to enlarge its directivity bandwidth. IEEE Ant Wireless Propag Lett 12:421–424

Thal H (2006) New radiation Q limits for spherical wire antennas. IEEE Trans Ant Propag 54:2757–2763

Veselago VG (1968) Experimental demonstration of negative index of refraction. Sov Phys Usp 47:509–514

White CR, Colburn JS, Nagele RG (2012) A non-Foster VHF monopole antenna. IEEE Ant Wireless Propag Lett 21:584–587

Wu BI, Wang W, Pacheco J, Chen X, Grzegorczyk T, Kong JA (2005) A study of using metamaterials as antenna substrate to enhance gain. Progress in Electromagnetics Research, PIER 51, EMW Publishing, Cambridge, MA, pp 295–328

Yaghjian AD, Best SR (2005) Impedance, bandwidth, and Q of antennas. IEEE Trans Ant Propag 53:1298–1324

Yaghjian AD, Stewart HR (2010) Lower bounds on the Q of electrically small dipole antennas. IEEE Trans Ant Propag 58:3114–3121

Yang F, Rahmat-Samii Y (2009) Electromagnetic band gap structures in antenna engineering. Cambridge University Press, New York

Zhu J, Antoniades MA, Eleftheriades GV (2010) A compact tri-band monopole antenna with single-cell metamaterial loading. IEEE Trans Ant Propag 244:1031–1038

Zhu N, Ziolkowski RW (2011) Active metamaterial-inspired broad bandwidth, efficient, electrically small antennas. IEEE Ant Wireless Propag Lett 10:1582–1585

Zhu N, Ziolkowski RW (2012a) Design and measurements of an electrically small, broad bandwidth, non-Foster circuit-augmented protractor antenna. Appl Phys Lett 101:024107

Zhu N, Ziolkowski RW (2012b) Broad bandwidth, electrically small antenna augmented with an internal non-Foster element. IEEE Ant Wireless Propag Lett 11:1116–1120

Zhu N, Ziolkowski RW (2013) Broad bandwidth, electrically small, non-Foster element-augmented antenna designs, analyses, and measurements. IEICE Trans Commun E96-B:2399–2409

Ziolkowski RW (2003) Design, fabrication, and testing of double negative metamaterials. IEEE Trans Ant Propag 51:1516–1529

Ziolkowski RW, Kipple A (2003) Application of double negative metamaterial to increase the power radiated by electrically small antennas. IEEE Trans Ant Propag 51:2626–2640

Ziolkowski RW (2004) Propagation in and scattering from a matched metamaterial having a zero index of refraction. Phys Rev E 70:046608
Ziolkowski RW, Kipple A (2005) Reciprocity between the effects of resonant scattering and enhanced radiated power by electrically small antennas in the presence of nested metamaterial shells. Phys Rev E 72:036602
Ziolkowski RW, Erentok A (2006) Metamaterial-based efficient electrically small antennas. IEEE Trans Ant Propag 54:2113–2130
Ziolkowski RW, Erentok A (2007) At and beyond the Chu limit: passive and active broad bandwidth metamaterial-based efficient electrically small antennas. IET Microwav Ant Propag 1:116–128
Ziolkowski RW (2008a) An efficient, electrically small antenna designed for VHF and UHF applications. IEEE Ant Wireless Propag Lett 7:217–220
Ziolkowski RW (2008b) Efficient electrically small antenna facilitated by a near-field resonant parasitic. IEEE Ant Wireless Propag Lett 7:580–583
Ziolkowski RW, Jin P (2008) Metamaterial-based dispersion engineering to achieve phase center compensation in a log-periodic array. IEEE Trans Ant Propag 56:3619–3629
Ziolkowski RW, Lin CC, Nielsen JA, Tanielian MH, Holloway CL (2009a) Design and experimental verification of a 3D magnetic EZ antenna at 300 MHz. IEEE Ant Wireless Propag Lett 8:989–993
Ziolkowski RW, Jin P, Nielsen JA, Tanielian MH, Holloway CL (2009b) Design and experimental verification of Z antennas at UHF frequencies. IEEE Ant Wireless Propag Lett 8:1329–1333
Ziolkowski RW, Jin P, Lin CC (2011) Metamaterial-inspired engineering of antennas. Proc IEEE 99:1720–1731
Ziolkowski RW, Tang MC, Zhu N (2013) An efficient, broad bandwidth, high directivity, electrically small antenna. Microw Opt Technol Lett 55:1430–1434